GEOCHEMISTRY

Nitrate limitation in early Neoproterozoic oceans delayed the ecological rise of eukaryotes

Junyao Kang[1,2], Benjamin Gill[1,2], Rachel Reid[1,2], Feifei Zhang[3], Shuhai Xiao[1,2]*

The early Neoproterozoic Era witnessed the initial ecological rise of eukaryotes at ca. 800 Ma. To assess whether nitrate availability played an important role in this evolutionary event, we measured nitrogen isotope compositions ($\delta^{15}N$) of marine carbonates from the early Tonian (ca. 1000 Ma to ca. 800 Ma) Huaibei Group in North China. The data reported here fill a critical gap in the $\delta^{15}N$ record and indicate nitrate limitation in early Neoproterozoic oceans. A compilation of Proterozoic sedimentary $\delta^{15}N$ data reveals a stepwise increase in $\delta^{15}N$ values at ~800 Ma. Box model simulations indicate that this stepwise increase likely represents a ~50% increase in marine nitrate availability. Limited nitrate availability in early Neoproterozoic oceans may have delayed the ecological rise of eukaryotes until ~800 Ma when increased nitrate supply, together with other environmental and ecological factors, may have contributed to the transition from prokaryote-dominant to eukaryote-dominant marine ecosystems.

INTRODUCTION

Although eukaryotes as a clade likely diverged from their living sister clade in the Paleoproterozoic, they did not become phylogenetically and ecologically diverse until sometime in the Tonian Period [1000 to 720 million years (Ma)] (1–3). The delayed transition from a prokaryote-dominant to a eukaryote-dominant marine ecosystem marks an important milestone in the evolutionary history of the biosphere and is documented by multiple lines of evidence. First, phylogenetically resolved crown-group eukaryotes, including the red alga *Bangiomorpha pubescens* and the green alga *Proterocladus antiquus*, emerged in the Tonian Period ca. 1.0 billion years (Ga) (1). Various micro-/macrofossils also indicate that important eukaryotic evolutionary innovations occurred during this time, including multicellularity, cell differentiation, biomineralization, and eukaryovory (4). Furthermore, there is an increase in global species richness in the late Tonian Period (ca. 800 Ma) (5), although an increase of within-assemblage fossil diversity is not apparent (4). The morphological disparity of eukaryotic fossils also expanded in the Tonian Period relative to the preceding Mesoproterozoic Era (6). Lipid biomarkers (see discussion in the Supplementary Materials) suggest an ecological rise of eukaryotic primary producers during the Tonian Period [(7), but see (8)].

What factors may have driven the transition from a prokaryote-dominant to a eukaryote-dominant marine ecosystem? Given the coupling of predation and animal diversity (9, 10), it is possible that the rise of eukaryovory may have driven the phylogenetic diversification of eukaryotes in the Tonian (5, 11). However, this hypothesis does not account for the ecological dominance of eukaryotes, which is likely also linked to nutrient supplies and the rise of eukaryotic primary producers. Phosphorus has long been regarded as the ultimate limiting nutrient on geological time scales (12). It has been proposed that an enlarged marine phosphorus reservoir

after the Sturtian glaciation in the Cryogenian (13) was responsible for the ecological rise of eukaryotic algae as the dominant primary producers (7). Widespread ferruginous conditions in pre-Cryogenian oceans may have caused marine phosphorus limitation due to enhanced phosphorus scavenging into the sediment by iron minerals (13) and weakened phosphorus remineralization in anoxic environments (14). Under such conditions, cyanobacteria outcompete phototrophic eukaryotes because of their smaller cell size and greater efficiency of nutrient uptake (7, 15). During the Cryogenian, enhanced postglacial weathering likely introduced a substantial amount of phosphorus into the ocean (13, 16). With increased phosphate availability, eukaryotic phototrophs became more competitive than cyanobacteria, and the ecological rise of eukaryotic algae with a larger cell size led to a more efficient biological pump and fundamental changes in the marine carbon cycle and redox structure (13, 16).

In principle, the bioavailability of nitrogen, another macronutrient in marine ecosystems, could have also played a similar role in driving the ecological rise of eukaryotic primary producers. It has been suggested that fixed nitrogen, instead of phosphorus, limits primary productivity on glacial-to-interglacial time scales (17). Earth system models show that bioavailable nitrogen may have been a limiting nutrient during parts of the Proterozoic when $p\text{O}_2$ (partial pressure of oxygen) was at intermediate levels of 0.1× to 0.4× present atmospheric level (13). The marine biogeochemical cycle of nitrogen, which has multiple redox states, is closely coupled with oceanic redox structures. Nitrogen fixation reduces atmospheric N_2 to biologically accessible ammonium. In the presence of O_2, even at nanomolar levels (18), ammonium is oxidized to nitrate through nitrification. In suboxic-to-anoxic seawater and sedimentary porewaters, however, nitrate is reduced to gaseous species and removed from the ocean mainly through denitrification and anammox (19, 20). The availability of nitrate has long been regarded as a key factor dictating the competition between eukaryotic and bacterial primary producers (21). Eukaryotes do not fix nitrogen, and thus, their growth is dependent on the assimilation of bioavailable nitrogen (22). In contrast, diazotrophic cyanobacteria fix nitrogen whenever needed, although they can also release enzymes

[1]Department of Geosciences, Virginia Tech, Blacksburg, VA, USA. [2]Global Change Center, Virginia Tech, Blacksburg, VA, USA. [3]State Key Laboratory for Mineral Deposits Research, School of Earth Sciences and Engineering, and Frontiers Science Center for Critical Earth Material Cycling, Nanjing University, Nanjing 210023, China.
*Corresponding author. Email: xiao@vt.edu

to efficiently scavenge bioavailable nitrogen from the seawater (21). Thus, cyanobacteria can outcompete photosynthetic eukaryotes and maintain ecological dominance when nitrate is limited, but eukaryotes have an upper hand when nitrate is readily available, due to their ability to rapidly transport nitrate into the cell for further assimilation (23) and to store nitrate in intracellular vacuoles (21, 24). This nitrate-controlled dichotomy is readily seen in modern oceans, where diatoms dominate in nitrate-rich areas and cyanobacteria in nitrate-limited areas (Fig. 1). With low atmospheric oxygen levels and widespread anoxic conditions in the pre–800 Ma oceans (25–27), it is expected that nitrogen loss may be extensive and nitrate was not widely available (28). Therefore, it is possible that nitrate availability may be as important as phosphorus supply in limiting or fueling the ecological rise of photosynthetic eukaryotes. However, the current understanding of the early Neoproterozoic nitrogen cycle is extremely limited due to a lack of data, particularly for the early Tonian Period, prompting us to generate data from the Huaibei Group and to integrate a modeling approach to elucidate the potential role of nitrate in this critical evolutionary event.

To fill the early Tonian gap of $\delta^{15}N$ data, we investigated the ca. 1000 to 800 Ma Huaibei Group from the North China Craton (NCC), using a multi-geochemical proxy approach (Fe speciation and N isotopes). The Huaibei Group offers a window onto the shallow marine redox structure and nitrogen cycle before the proliferation of eukaryotic algae. Noting that $\delta^{15}N$ can be influenced by local environmental conditions and can show appreciable spatial variations (29, 30), we compiled a Proterozoic $\delta^{15}N$ database,

which was then analyzed using time series techniques to identify secular trends from local signals. Last, we used a simple box model to provide a broader view of nitrate availability and its potential relationship with the ecological rise of eukaryotes. This integrative approach helps us to quantitatively understand the early Neoproterozoic nitrogen cycle and to evaluate the possibility of a nitrate driver for the ecological rise of eukaryotes.

Geological background

The NCC is a major tectonic unit in China and one of the best studied cratons in the world. Tonian sedimentary rocks, including the Huaibei Group, occur in the Xuhuai rift system along the southeastern margin of the NCC. The Huaibei Group consists of 13 formations and can be divided into three parts (fig. S1), with eukaryotic fossils reported from the middle and upper parts of the group. The lower part of the succession consists of the Lanling, Xinxing, and Jushan formations that are predominantly siliciclastic rocks, including quartz sandstone and shale with carbonate concretions. The middle-upper Huaibei Group is dominated by carbonate rocks and consists of the Jiayuan, Zhaowei, Niyuan, Jiudingshan, Zhangqu, Weiji, and Shijia formations. Stromatolites and molar-tooth structures are common in this part of the succession, and putative vase-like microfossils, leiospheric acritarchs, *Chuaria*, and *Tawuia* have also been reported from this portion of the Huaibei Group (31). The upper part of the succession consists of the Wangshan Formation (stromatolitic dolostone and limestone), the Jinshanzhai Formation (quartz sandstone, shale, limestone, and
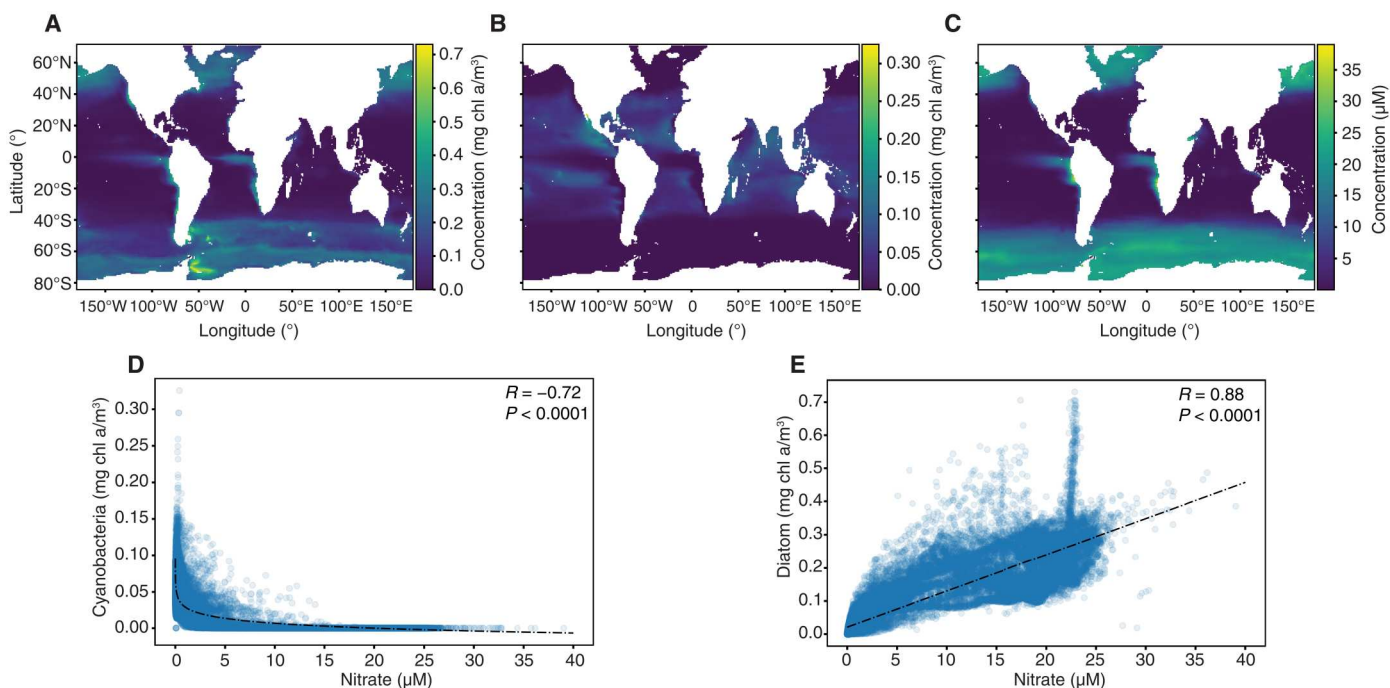

Fig. 1. Distribution of diatoms, cyanobacteria, and nitrate in modern oceans. (**A** to **C**) Time-averaged (January 2011 to December 2015) concentration maps of first major feature (the most prominent distribution pattern) of diatom (A), cyanobacteria (B), and nitrate (C). Major spatial features were extracted using singular value decomposition (see the Supplementary Materials). Note that maps show concentrations in first major features rather than actual concentrations in oceans. Concentration data are from NOBM (78). (**D** and **E**) Cross-plots of cyanobacteria (D) and diatom (E) versus nitrate concentrations in modern oceans, showing that diatoms are abundant in nitrate-rich areas, whereas cyanobacteria are dominant in nitrate-limited areas. Time-averaged data of the first major component were used in the plots. For diatom and nitrate, simple linear regression model ($y = a + b*x$) was applied. For cyanobacteria, log function [$y = a + b*\log(x)$] was applied. R and P values were calculated using Pearson correlation coefficient.

stromatolitic dolostone), and the uppermost Gouhou Formation (shale and siltstone) (32). The carbonaceous compression fossils *Chuaria*, *Tawuia*, and *Protoarenicola* have been reported from the Jinshanzhai Formation, and *Chuaria*, *Tawuia*, *Dictyosphaera* sp., *Trachyhystrichosphaera aimika*, and *Valeria lophostriata* have been recovered from the Gouhou Formation (31, 33). The exceptional fossil preservation suggests low degrees of thermal maturity (33), which is consistent with relatively low vitrinite reflectance (R_0: 2.2 to 2.5) of the Huaibei Group (34) and Raman spectroscopic data of organic-walled microfossils from age-equivalent strata in the same rift system (35).

The depositional age of the Huaibei Group is relatively well constrained by available radiometric, biostratigraphic, and chemostratigraphic data (fig. S1). Authigenic monazite from the Xinxing Formation gives a SIMS Pb–Pb age of 1086 ± 17 Ma, which is taken as an approximation of the initial depositional age of the Huaibei Group (36). Dolerite sills intruding the Wangshan Formation are dated at 906 ± 10 Ma (37), providing minimum age constraints on the intruded strata. The authigenic xenotime from the Shijia Formation suggest a minimum depositional age of 919 ± 23 Ma (36). These ages constrain most of the Huaibei Group between ~1086 and ~906 Ma. On the basis of an age model using strontium isotope chemostratigraphy, the deposition of most of the carbonate strata occurred between ca. 980 Ma and ca. 920 Ma (38). However, the youngest detrital zircons from the Jinshanzhai Formation yield a maximum depositional age of 820 ± 11 Ma (39), and the existence of *Protoarenicola* in the same formation suggests a Tonian age (>720 Ma). Hence, a ~100-Ma unconformity may be present between the Wangshan and the Jinshanzhai formations, and therefore, in this study, we assigned a <820-Ma age to the Jinshanzhai Formation. The presence of *T. aimika*, *V. lophostriata*, and *Dictyosphaera* sp. in the Gouhou Formation, *Protoarenicola* in the Jinshanzhai Formation, *Pararenicola* in the Shijia Formation, and *Tawuia* at multiple horizons in the Huaibei Group supports a Tonian age for this group. The $\delta^{13}C_{carb}$ chemostratigraphy is also consistent with the Tonian global $\delta^{13}C$ record (31).

In this study, we focus on the middle and upper parts of the Huaibei Group, which were mostly deposited on a shallow-water carbonate platform (40). Development of storm deposits, ripple marks, and cross-stratification suggests extensive mixing of the water column (41). In addition, paleontological data from the Jinshanzhai and Gouhou formations also indicate an open marine environment (33). A total of 141 carbonate samples were collected from four sections in the Huaibei region of North China, including the Zhaowei section (Jiayuan, Zhaowei, Niyuan, and Jiudingshan formations), Liangtang section (Jiudingshan Formation), Lushan section (Zhangqu, Weiji, and Shijia formations), and Langan section (upper Wangshan, Jinshanzhai, and Gouhou formations). These samples were analyzed for iron speciation and nitrogen isotope composition.

Iron speciation

Iron speciation is a widely used approach to evaluate local redox conditions in ancient sedimentary basins. This proxy focuses on iron species that are highly reactive (Fe_{HR}) toward dissolved sulfide, including iron in carbonate (Fe_{carb}), iron oxides (Fe_{ox}), magnetite (Fe_{mag}), and iron that has reacted with dissolved sulfide to form pyrite (Fe_{py}) (42). In sediments deposited under an anoxic water column, enrichment of highly reactive iron occurs via shelf-to-basin iron transport, resulting in elevated ratios of Fe_{HR} to the total iron (Fe_T) in the sediment (43). It has been shown, through analyses of modern and ancient sediments, that $Fe_{HR}/Fe_T < 0.22$ is indicative of sediments deposited under oxic water columns, and $Fe_{HR}/Fe_T > 0.38$ is indicative of sediments deposited under anoxic water columns. Furthermore, ferruginous (anoxic, iron-replete) and euxinic (anoxic, sulfide-replete) water columns can be distinguished using Fe_{py}/Fe_{HR} ratios, because proportionally more Fe_{HR} would react with hydrogen sulfide and precipitate as pyrite in the euxinic water columns than in ferruginous conditions. A threshold Fe_{py}/Fe_{HR} of 0.7 to 0.8 is widely used to separate ferruginous (<0.7) from euxinic conditions (>0.8) (42). More recently, with Holocene data from the eastern Mediterranean Sea (44), a lower threshold (0.6 to 0.8) has been suggested (45). While the iron speciation proxy was initially applied in the analysis of fine-grained siliciclastic rocks, recent work demonstrates that Fe_{HR}/Fe_T is also a reliable redox proxy for carbonate rocks with $Fe_T > 0.5$ weight % (wt %) (46). Here, we compiled a Fe speciation dataset of carbonate samples ($Fe_T > 0.5$ wt %) from modern and ancient anoxic basins to further evaluate the effectiveness of Fe_{py}/Fe_{HR} in carbonate rocks (see the Supplementary Materials).

The nitrogen isotope proxy

The nitrogen isotope composition ($\delta^{15}N$) of sedimentary rocks is a powerful tool for understanding the ancient nitrogen cycle. Sedimentary nitrogen has a biological origin and ultimately comes from primary producers (19, 20). Primary producers assimilate nitrogen from seawater and hence reflect the $\delta^{15}N$ of the ocean reservoir. In the ocean system, bioavailable nitrogen is ultimately supplied by N_2 fixation and removed by a combination of pathways, including heterotrophic denitrification and anammox in the water column and sediments, as well as the burial of nitrogen in sediments. On geologic time scales, the $\delta^{15}N$ of the ocean reservoir is controlled by the isotopic fractionation associated with these input and output fluxes. For the input flux, nitrogen fixation is associated with a small fractionation ($\varepsilon_{NH_4^+-N_2}$) of −2‰ to +1‰ when Mo-based nitrogenase enzyme is used (19). Alternative pathways using V-/Fe-based nitrogenases can cause fractionations of −6 to −8‰; however, on the basis of the nitrogen isotope record and phylogenetic data, these enzymes are thought to be negligible in Precambrian oceans (19, 47). Given the $\delta^{15}N$ of atmospheric N_2 ($\delta^{15}N = 0$‰) (48), in a fully anoxic ocean (Fig. 2A) where ammonium is the dominant species and assimilation is quantitative (i.e., nitrate is completely removed) (19), a near-zero (−2 to +1‰) $\delta^{15}N$ for marine sediments would be expected. On the other hand, when nitrate is abundant (Fig. 2, B and C), its partial removal from the water column through denitrification and anammox can impart substantial isotopic fractionations of −10 to −30‰ ($\varepsilon_{N_2-NO_3^-}$) (49), leading to ^{15}N enrichment in the residual nitrate pool. When denitrification/anammox occurs in the sediments, however, nitrate loss is quantitative and the net isotopic fractionation approaches 0‰ (49). The nitrate $\delta^{15}N$ signals are then transferred to sediments by organisms assimilating nitrate as the nitrogen source. As shown in Fig. 2 (B and C), nitrogen cycles in a Proterozoic ocean with oxygenated surface water and in the modern ocean with an oxygen minimum zone are similar. The major difference is the extent of nitrogen removal and therefore the size of nitrate reservoir. In modern oceans, the average $\delta^{15}N$ value of sediments is

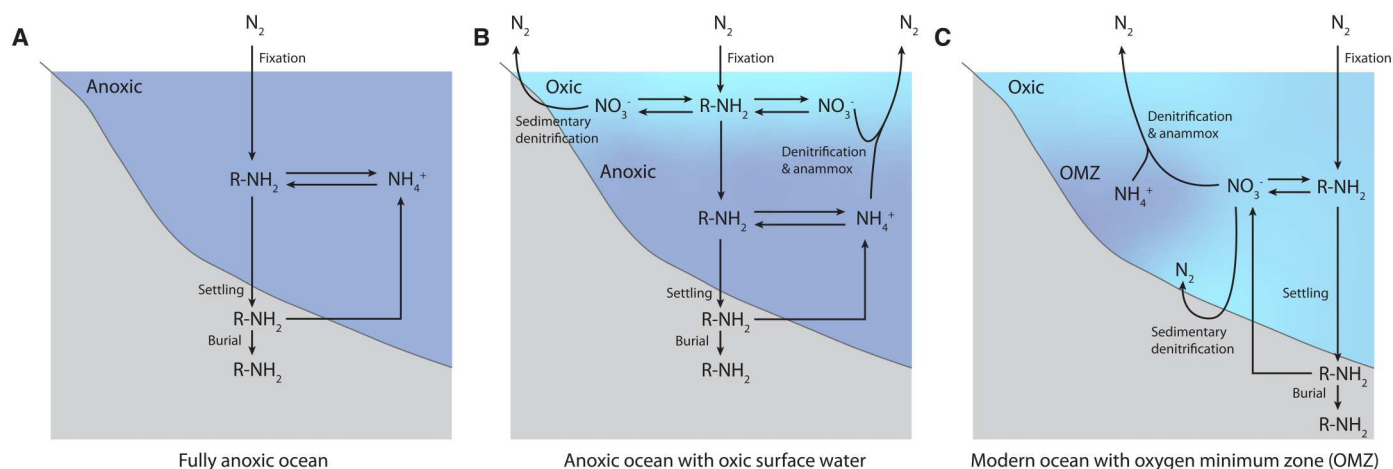**Fig. 2. Simplified nitrogen cycles in Precambrian and modern oceans.** R-NH$_2$ represents organic nitrogen. (**A**) Nitrogen cycle in a fully anoxic ocean (e.g., in much of the Archean). Arrows between organic nitrogen and ammonium represent ammonification and nitrogen assimilation processes. (**B**) Nitrogen cycle in an anoxic ocean with oxic surface water (e.g., in much of the Proterozoic). Arrows from organic nitrogen to nitrate represent a combination of ammonification and nitrification processes. Arrows from nitrate to organic nitrogen represent the nitrogen assimilation process. (**C**) Nitrogen cycle in the modern ocean with an oxygen minimum zone (OMZ).

about +5‰ due to partial nitrate loss in oxygen minimum zones (*29*), whereas average δ^{15}N of Proterozoic sediment is expected to be lower (but still above 0‰) due to stronger nitrate loss and proportionally greater ammonium assimilation. In summary, positive δ^{15}N values of sediments can be regarded as evidence for nitrate availability in the contemporaneous oceans, and near-zero δ^{15}N values indicate nitrate scarcity and/or extensive nitrogen loss.

On the basis of previous nitrogen cycle models (*50*, *51*), we applied a steady-state box model to understand how nitrate availability in the ocean affects nitrogen isotope signals preserved in sediments (fig. S2). Because our focus is the evolution of the nitrate reservoir on geological time scales (>10^6 years), steady-state models are appropriate (*50*, *51*). In addition, because the box model does not capture spatial heterogeneity and temporal dynamics, the simulated outputs only represent global averages. In this model, two nitrogen reservoirs were considered (fig. S2) (*51*). The first reservoir (N$_{fixer}$/ammonium) includes organic nitrogen of diazotrophic organisms (N$_{fixer}$, mostly cyanobacteria) and ammonium derived from the remineralization of this organic matter. The second reservoir (N$_{assimilator}$/nitrate) includes nitrate and organic nitrogen of nitrate-assimilating organisms (N$_{assimilator}$, mostly eukaryotes). We only considered net input and output fluxes related to these two reservoirs. For example, although dissimilatory nitrate reduction to ammonium was argued to be important in Proterozoic ferruginous oceans (*52*), this nitrogen transformation pathway is not included in our model because it is a recycling flux that is accounted for when the net nitrification is parameterized. For the N$_{fixer}$/ammonium reservoir, the only input flux is N$_2$ fixation (F_{fix}). A large portion of this input flux is balanced by net nitrification (F_{remin}) coupled with remineralization, which supplies nitrate to the second reservoir (N$_{assimilator}$/nitrate). Only a minor portion escapes from remineralization and is buried in marine sediments (F_{fixer_burial}). For the N$_{assimilator}$/nitrate reservoir, F_{remin} is the major input, with two minor input fluxes (atmospheric deposition F_{depo} and riverine input F_{river}). In this study, F_{depo} and F_{river} were considered when the model was validated by reproducing modern ocean δ^{15}N values (see the Supplementary Materials). However,

because these two fluxes are orders of magnitude smaller than F_{fix} and their impact on model results is negligible (*51*), they were not considered when modeling the Precambrian nitrogen cycle. The major output fluxes from the N$_{assimilator}$/nitrate reservoir are denitrification/anammox in the water column (F_{wcd}) and sediments (F_{sd}), with a minor part of N$_{assimilator}$ buried and preserved as sedimentary N ($F_{assimilator\_burial}$). In our model, F_{sd} was held as a constant equivalent to its modern value, because even surface sediments under oxic water columns can reach the denitrification zone (*53*). Ultimately, the ratio of F_{sd} to F_{wcd} controls δ^{15}N of the nitrate reservoir (N$_{assimilator}$/nitrate). We note that in extreme cases where marine anoxia and water-column denitrification/anammox are prevalent, nitrate is exhausted in the water column and denitrification/anammox in the sediment is diminished. In such cases, it is inappropriate to hold F_{sd} at its modern value. Although not implemented in this model, in such extreme cases, isotopic fractionation associated with both water-column and sedimentary denitrification/anammox approaches to zero, and δ^{15}N of the nitrate reservoir (N$_{assimilator}$/nitrate) would be near zero and insensitive to F_{sd}/F_{wcd}.

When in steady state, the fluxes into and out of the ammonium and nitrate reservoirs can be described as follows (Eqs. 1 and 2)

$$F_{fix} = F_{remin} + F_{fixer\_burial} \tag{1}$$

$$F_{remin} = F_{wcd} + F_{sd} + F_{assimilator\_burial} \tag{2}$$

The isotope mass balance can be described in Eqs. 3 and 4

$$F_{fix} \times (\delta^{15}N_{atmo} + \varepsilon_{fix}) = F_{remin} \times \delta^{15}N_{fixer/ammonium} \\ + F_{fixer\_burial} \times \delta^{15}N_{fixer/ammonium} \tag{3}$$

$$F_{remin} \times \delta^{15}N_{fixer/ammonium} = F_{wcd} \times (\delta^{15}N_{assimilator/nitrate} + \varepsilon_{wcd}) \\ + F_{sd} \times (\delta^{15}N_{assimilator/nitrate} + \varepsilon_{sd}) + F_{assimilator\_burial} \\ \times \delta^{15}N_{assimilator/nitrate} \tag{4}$$

where $\delta^{15}N_{atmo}$, $\delta^{15}N_{fixer/ammonium}$, and $\delta^{15}N_{assimilator/nitrate}$ are nitrogen isotope compositions of atmospheric N_2, N_{fixer}/ammonium reservoir, and $N_{assimilator}$/nitrate reservoir, respectively, and ε_{fix}, ε_{wcd}, and ε_{sd} are fractionation factors associated with F_{fix}, F_{wcd}, and F_{sd}, respectively (see the Supplementary Materials for the parameterization of ε_{fix}, ε_{wcd}, and ε_{sd}, which are defined as $\varepsilon = \delta^{15}N_{product} - \delta^{15}N_{reactant}$). Fractionations associated with denitrification and anammox are not differentiated and are represented by a single fractionation factor that integrates both denitrification and anammox, as is commonly done in field site measurements ([49]). This choice is also supported by culture experiments showing similar isotopic effect of denitrification and anammox ([54]). Furthermore, we assumed no isotopic fractionation associated with F_{remin}, $F_{assimilator\_burial}$, and F_{fixer_burial} ([19, 20, 51]). Solving Eqs. 1 to 4, we can obtain the nitrogen isotope compositions of the two oceanic reservoirs (Eqs. 5 and 6)

$$\delta^{15}N_{fixer/ammonium} = \delta^{15}N_{atmo} + \varepsilon_{fix} \qquad (5)$$

$$\delta^{15}N_{assimilator/nitrate} = \delta^{15}N_{fixer/ammonium} - (F_{wcd} \times \varepsilon_{wcd} + F_{sd} \times \varepsilon_{sd})/F_{remin} \qquad (6)$$

Because nitrate is the focus of this study, we formulated $f_{assimilator}$ (Eq. 7) as the proportion of nitrogen that is buried from the $N_{assimilator}$/nitrate reservoir. Thus, $f_{assimilator}$ can be viewed as an indicator of nitrate availability in the ocean; when nitrate level is high, we expect a greater $f_{assimilator}$ value or a larger contribution of nitrate burial to the total nitrogen burial.

$$f_{assimilator} = F_{assimilator\_burial}/F_{total\_burial} \qquad (7)$$

As the total burial flux (F_{total_burial}) is a mixture of F_{fixer_burial} and $F_{assimilator\_burial}$, the nitrogen isotope composition of sediments
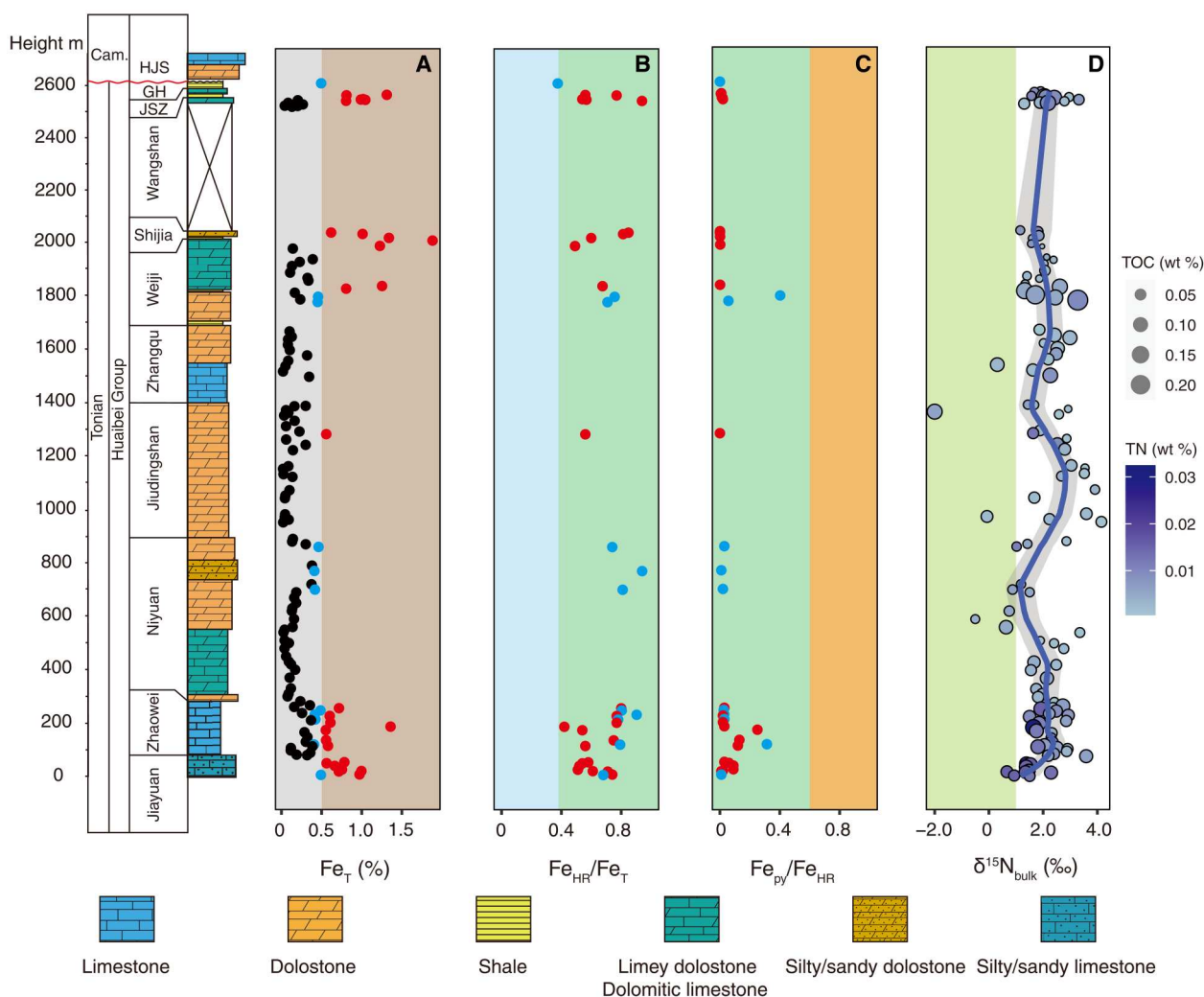

Fig. 3. Geochemical data from the Huaibei Group. Red points in (**A**) to (**C**) denote samples with $Fe_T > 0.5\%$; blue points, Fe_T 0.4 to 0.5%; black points, $Fe_T < 0.4\%$. Blue band in (B) marks sediments deposited under oxic conditions, and green band marks sediments deposited under anoxic conditions. In (C), green band represents ferruginous conditions, and orange band represents euxinic conditions. In (D), green band marks near-zero $\delta^{15}N_{bulk}$ values indicative of dominance of nitrogen fixation. Color and size of data points are keyed to reflect TN and TOC contents. Blue line is LOWESS regression fit with 95% CI (gray shadow) calculated from SEs.

($\delta^{15}N_{sed}$) can be expressed as follows (Eq. 8)

$$\delta^{15}N_{sed} = (1 - f_{assimilator}) \times \delta^{15}N_{fixer/ammonium} + f_{assimilator} \\ \times \delta^{15}N_{assimilator/nitrate} \qquad (8)$$

Because both $F_{assimilator\_burial}$ and nitrate loss through denitrification/anammox are controlled by the extent of anoxia in the ocean, $F_{assimilator\_burial}$ is expected to decrease when nitrate loss increases. We thus added an extra constraint on $F_{assimilator\_burial}$ (Eq. 9) (51)

$$F_{assimilator\_burial} \propto \frac{1}{F_{total\_denit}} \qquad (9)$$

where $F_{total\_denit} = F_{wcd} + F_{sd}$. Because our focus is on $f_{assimilator}$ or $F_{assimilator\_burial}$ as a proportion of F_{total_burial} (Eq. 7), we used a constant F_{total_burial} (= 25 Tg/year) in our model calculation. We varied $f_{assimilator}$ from 0 to 100% to understand how variation in nitrate availability would affect $\delta^{15}N_{sed}$. Last, the uncertainty of ϵ_{fix} and ϵ_{wcd} was evaluated using a Monte Carlo simulation in which ϵ_{fix} and ϵ_{wcd} were sampled from uniform distributions (ϵ_{fix}, −2 to 1‰; ϵ_{wcd}, −30 to −22‰). Although higher ϵ_{wcd} values (−15 to −10‰) have been reported from cellular-level culture experiments (55), we used community fractionation factors from field studies to better capture global average conditions.

RESULTS

Twenty-five samples with Fe_T greater than 0.5% and 11 samples with Fe_T between 0.4 and 0.5% were analyzed for iron speciation (Fig. 3A). All of these samples have Fe_{HR}/Fe_T greater than 0.38 (average, 0.68; range, 0.38 to 0.94) and Fe_{py}/Fe_{HR} less than 0.6 (average, 0.05; range, 0 to 0.40) (Fig. 3, B and C).

The compilation of Fe speciation data from carbonate deposits in modern and ancient anoxic basins (Fig. 4), where inference of redox condition was based on independent proxies (e.g., redox-sensitive trace metal concentrations) or Fe speciation data from adjacent beds of fine-grained siliciclastic sediments (table S1), shows that carbonate samples with $Fe_T > 0.5$ wt % can be used in iron speciation analysis for paleo-redox investigation (see the Supplementary Materials). The compilation also validates the recently revised threshold of Fe_{py}/Fe_{HR} = 0.6 to 0.8 (45) for the differentiation of ferruginous and euxinic conditions based on carbonate samples with $Fe_T > 0.5$ wt % . In light of this, carbonate samples from the Huaibei Group with $Fe_T > 0.5$ wt % provide reliable Fe speciation data, whereas those with Fe_T between 0.4 and 0.5 wt % are considered, but with caution.

A total of 123 carbonate samples from the Huaibei Group were decarbonated and the residues were analyzed for total organic carbon content (TOC), total nitrogen content (TN), organic carbon isotope composition ($\delta^{13}C_{TOC}$), and total nitrogen isotope composition ($\delta^{15}N_{bulk}$) (Fig. 3D and fig. S3). Average TOC is 0.05 wt % (ranging from 0.01 to 0.21 wt %, $n = 123$), average TN is 0.006 wt % (ranging from 0.001 to 0.032 wt %, $n = 112$), average $\delta^{13}C_{TOC}$ is −27.0‰ (ranging from −29.8 to −19.8‰, $n = 123$), and average $\delta^{15}N_{bulk}$ is 2.0‰ (ranging from −2.0 to 4.2‰, $n = 112$). About 74% of the samples have $\delta^{15}N_{bulk}$ less than 2.5‰ ($n = 83$), and ~54% samples have $\delta^{15}N_{bulk}$ between 1.5 and 2.5‰ ($n = 61$). A positive excursion was observed in the Jiudingshan Formation, where $\delta^{15}N_{bulk}$ rises from 1.4 to 4.2‰ and then declines to

1.7‰. Short-term fluctuations of $\delta^{15}N_{bulk}$ values were also observed in this section.

Numerical modeling results show that $\delta^{15}N_{sed}$ has a nonlinear relationship with the proportional contribution of nitrate-assimilating eukaryotes ($f_{assimilator}$) to sedimentary nitrogen. $\delta^{15}N_{sed}$ values are highest when $f_{assimilator}$ is ~0.5 but decrease to near-zero values when $f_{assimilator}$ approaches zero or unity (Fig. 5E). When $f_{assimilator}$ approaches zero, the ocean is mostly anoxic and nitrate is not available. Sedimentary nitrogen is largely derived from nitrogen-fixing cyanobacteria, which have near-zero $\delta^{15}N$ values. When $f_{assimilator}$ approaches unity, the ocean is mostly oxic and water-column denitrification/anammox approaches zero. As a result, $\delta^{15}N_{assimilator/nitrate}$ and sedimentary $\delta^{15}N$ approach 0‰.

The modeling results also show that modeled $\delta^{15}N_{sed}$ is affected by the fractionation factor associated with nitrogen fixation [ϵ_{fix}, allowed to vary between −2 and +1‰ (51)] and the fractionation factor associated with water-column denitrification/anammox [ϵ_{wcd}, allowed to vary between −30 and −22‰ (49)] (Fig. 5, A to D). Briefly, as ϵ_{fix} increases, heavier nitrogen is introduced to the ocean through nitrogen fixation and $\delta^{15}N_{sed}$ reaches higher values. In contrast, as ϵ_{wcd} decreases, lighter nitrogen is removed from the ocean through water-column denitrification/anammox and $\delta^{15}N_{sed}$ reaches higher values.

The $\delta^{15}N$ data from the Huaibei Group were incorporated in a compilation of sedimentary nitrogen isotope data ($n = 1824$) from ~1.6 to ~0.539 Ga, which is updated from a database compiled by Stüeken et al. (19). The compiled dataset captures a wide range of marginal marine depositional environments to reflect the global nitrogen cycle. Data are grouped into 100-Ma time bins and plotted in Fig. 6A. The dataset is dominated by $\delta^{15}N$ data derived from fine-grained siliciclastic lithologies (1194 samples) as opposed to carbonate rocks (630 samples). This is especially true for the Mesoproterozoic data, with only 85 of 574 samples from carbonate rocks.

DISCUSSION
Evidence for primary oceanic signals
Previous petrographic, paleontological, and geochemical work on the same suite of samples analyzed here indicates excellent preservation of the sedimentary fabrics, minimal diagenetic alteration, and low degrees of thermal maturity (31, 56). Here, we further assess possible postdepositional alteration of the Fe speciation and $\delta^{15}N$ signals.

Fe speciation is subjected to diagenetic and metamorphic alterations because iron and sulfur can be removed from or added to the sediments after deposition. Given that most carbonate samples are micritic with no notable recrystallization or late-stage cements (31), postdepositional alteration is likely limited. One specific concern for the Fe speciation proxy is the reaction between highly reactive iron minerals and dissolved sulfide from diagenetic fluids, which could potentially elevate the Fe_{py}/Fe_{HR} of samples with $Fe_{HR}/Fe_T > 0.38$ and thus lead to false signals of euxinia (57). Because all analyzed samples have low pyrite contents and no euxinic signal is recorded in the Huaibei samples, this indicates that this bias is not a concern for our samples. Another form of postdepositional alteration comes from deep burial dolomitization, which introduces reactive iron from external sources (42) and elevates the Fe_{HR}/Fe_T ratio. However, previous studies have shown that dolomite in the Huaibei Group and many other Neoproterozoic
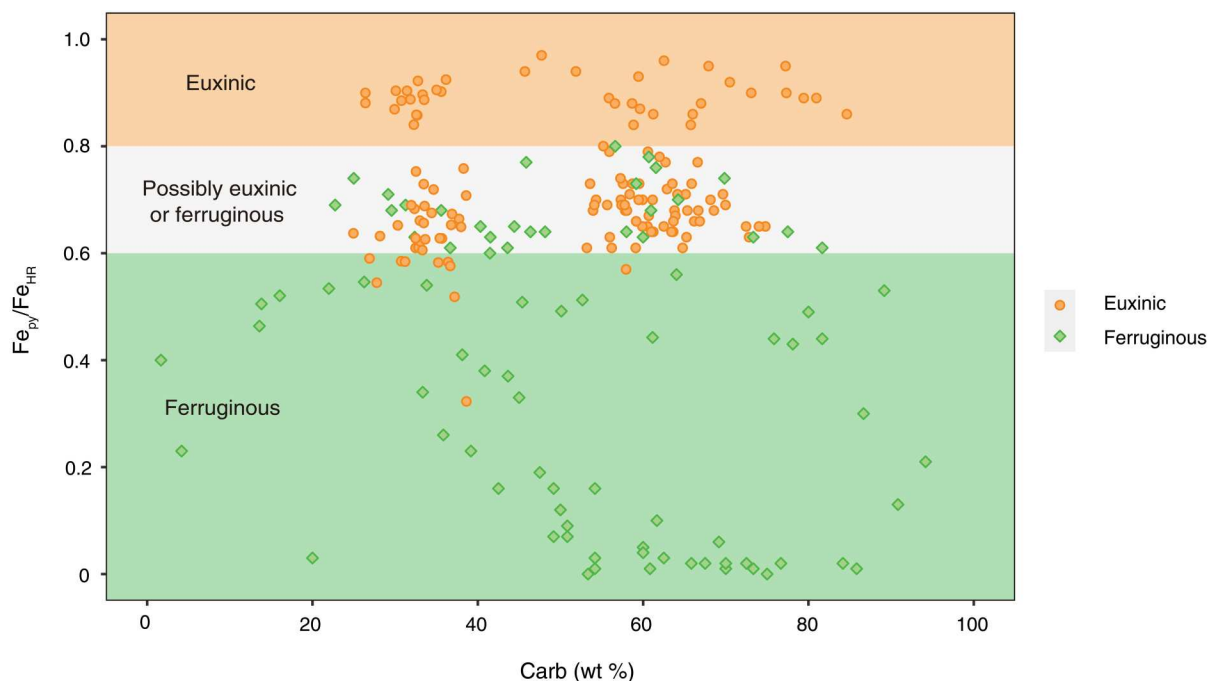
Fig. 4. Fe$_{py}$/Fe$_{HR}$ ratios plotted against carbonate percentage for independently assessed euxinic and ferruginous samples. Modern and ancient samples with Fe$_T$ ≥ 0.5% were plotted. The data compilation confirms that the recently proposed euxinic/ferruginous threshold (0.6 to 0.8) is valid for distinguishing euxinic versus ferruginous conditions in carbonate samples. See table S1 for data sources and independent assessment of redox conditions.

successions are likely syndepositional or early diagenetic (*58*, *59*), suggesting a lack of highly reactive iron input later during diagenesis. In addition, Fe$_{carb}$ is not correlated with Mg/Ca (fig. S4), indicating that dolomitization is not a major controlling factor on Fe$_{carb}$ and Fe$_{HR}$.

δ^{15}N signals in sedimentary organic matter can also be altered by diagenesis, metamorphism, and detrital contributions. Isotope modifications during biodegradation in the water column and in surface sediments are controlled by oxygen exposure time, which is related to dissolved oxygen content, water depth, and sedimentation rate. When oxygen exposure is limited, isotopic alteration during this process is negligible (<1‰) (*20*). Considering that the Huaibei carbonates were deposited on a shallow-water carbonate platform (where sedimentation rate tends to be high) and under ferruginous conditions (see discussion below), isotope alteration during early diagenesis is likely minimal. In late diagenesis, nitrogen can be removed from organic matter as NH$_4^+$ through either microbial remineralization or thermal maturation. This ammonium can be recaptured by clay minerals (as substitutes for monovalent cations) in the sediment or rock under closed system conditions (*60*). Instead of a net loss of sedimentary nitrogen, this process merely redistributes N between organic matter to clay minerals. Therefore, δ^{15}N of bulk samples (δ^{15}N$_{bulk}$, including both organic-N and clay-NH$_4^+$) remains relatively robust against diagenetic alteration. Regarding low-grade metamorphism (from anthracite to semigraphite stages), which is suggested by low vitrinite reflectance (*34*) and organic-walled microfossil preservation (*33*) in the Huaibei Group, previous studies have demonstrated that metamorphic denitrogenation can cause nitrogen loss but induces little isotopic fractionation (*20*). However, these studies focused on coal deposits with high organic matter contents (*20*). Because

progressive metamorphism causes preferential loss of N relative to C, and preferential loss of light isotopes (^{14}N and ^{12}C), correlations between δ^{15}N$_{bulk}$ and TN, δ^{15}N$_{bulk}$ and C/N, and δ^{15}N$_{bulk}$ and δ^{13}C$_{org}$ are expected (*51*). However, none of these correlations are observed in our data (fig. S5, A to C). Nitrogen from detrital clay minerals can also potentially mask the primary δ^{15}N signals. The strong correlation between TN and TOC of decarbonated samples (fig. S5D), however, indicates that TN is dominated by organic nitrogen, although the nonzero intercept does suggest that a small fraction of TN is derived from clay minerals. However, even this small amount of clay-bound nitrogen may have been, at least partially, recaptured nitrogen from the decomposition of organic matter.

Ferruginous shallow waters and nitrate limitation in the early Tonian Ocean

High Fe$_{HR}$/Fe$_T$ ratios (>0.38) but low Fe$_{py}$/Fe$_{HR}$ ratios (<0.6) of all Huaibei samples with Fe$_T$ > 0.5% indicate that the Huaibei carbonates were deposited under a persistently anoxic and ferruginous water column (Fig. 3). The development of ferruginous conditions in the Xuhuai rift basin is consistent with the previously published Fe speciation data from Tonian siliciclastic rocks in the adjacent Huainan region, which also indicate consistently ferruginous conditions elsewhere in the basin (*27*). Guilbaud *et al.* (*27*) argued for a transition from euxinic to ferruginous mid-depth waters in the earliest Tonian that was driven by a greater Fe$_{HR}$ flux into the oceans relative to that of sulfate, ultimately related to change in weathering regime during the amalgamation of Rodinia. Considering that the ferruginous conditions are recorded in carbonate rocks of the Huaibei Group deposited on a shallow-water carbonate platform, the chemocline must have been relatively shallow, at least in the
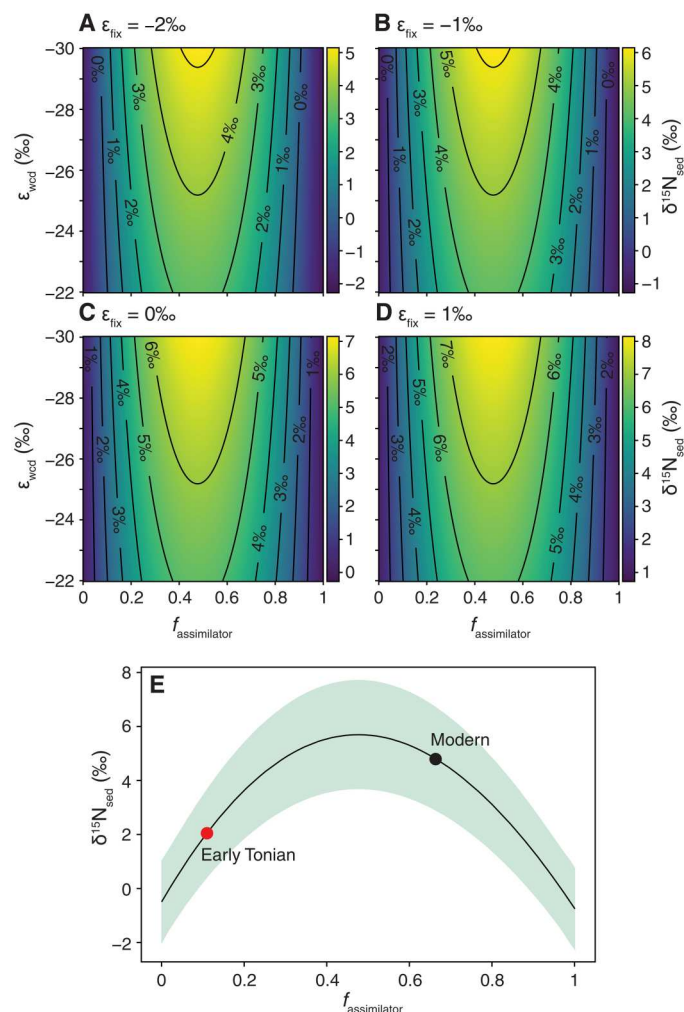
Fig. 5. Results of numerical modeling, showing effect of $f_{assimilator}$, ε_{fix}, and ε_{wcd} on $\delta^{15}N_{sed}$. (**A** to **D**) Model results showing effect of ε_{fix} and ε_{wcd} on sedimentary nitrogen isotope composition ($\delta^{15}N_{sed}$). Each plot shows modeled $\delta^{15}N_{sed}$ values with a fixed ε_{fix} value but variable ε_{wcd} values. When ε_{fix} is higher or ε_{wcd} is lower, $\delta^{15}N_{sed}$ becomes higher at a fixed $f_{assimilator}$; note that the ε_{wcd} axis is inverted. Relationship between $\delta^{15}N_{sed}$ and $f_{assimilator}$ is not linear: $\delta^{15}N_{sed}$ is highest at intermediate $f_{assimilator}$ values, but decreases when $f_{assimilator}$ approaches to zero (due to greater contribution from nitrogen-fixing organisms) or unity (due to weaker denitrification/anammox). (**E**) Modeled $\delta^{15}N_{sed}$ values with Monte Carlo sampling of ε_{fix} (−2 to 1‰, uniform distribution) and ε_{wcd} (−30 to −22‰, uniform distribution). Black line represents median values, and green shade shows 95% CI. In modern oceans, $f_{assimilator}$ is ~0.7 and $\delta^{15}N_{sed}$ is ~5‰ (black dot). $\delta^{15}N_{sed}$ of Huaibei Group samples is ~2.0‰ (red dot), and $f_{assimilator}$ is estimated to be <0.5 in more anoxic Tonian oceans.

Xuhuai rift basin. The expansion of ferruginous seawaters onto carbonate platforms is also in line with recently published uranium isotope data, which indicate extensive shallow-water anoxia on a global scale in the early Tonian Period (56).

As discussed above, ferruginous shallow waters would be expected to cause extensive nitrogen loss through denitrification and anammox, leading to a marine nitrogen cycle dominated by N-fixation and sedimentary N characterized by near-zero $\delta^{15}N$ values. The Huaibei Group has an average $\delta^{15}N_{bulk}$ of 2.0‰ (Fig. 3),

indicating extensive but not quantitative removal of nitrate through denitrification and anammox, which would likely result in nitrate limitation. Variations in $\delta^{15}N_{bulk}$ values throughout the Huaibei Group may be related to small-scale changes in the oxygen level of surface waters, while bottom waters maintained ferruginous conditions. The positive excursion in the Jiudingshan Formation probably represents a transient expansion of oxic shallow waters. These small-scale and transient variations are consistent with a small nitrate reservoir, which was sensitive to local changes in input or output fluxes.

On the basis of numerical modeling results (Fig. 5), a mean $\delta^{15}N_{bulk}$ of ~2.0‰ from the Huaibei Group would require a relatively low contribution from nitrate assimilators (mostly eukaryotes) to sedimentary nitrogen. These $\delta^{15}N_{bulk}$ values suggest $f_{assimilator}$ of only 0.11 (when $\varepsilon_{fix} = −0.5‰$ and $\varepsilon_{wcd} = −26‰$) on average; although $f_{assimilator}$ of 0.87 (when $\varepsilon_{fix} = −0.5‰$ and $\varepsilon_{wcd} = −26‰$) can mathematically satisfy the mass balance equations, this is inconsistent with the geochemical data indicative of shallow-water ferruginous anoxia and a relatively small marine nitrate reservoir. Under a scenario with high ε_{fix} (1‰) and low ε_{wcd} (−30‰), $f_{assimilator}$ would decrease further to 0.03. Even at relatively low ε_{fix} (−2‰) and high ε_{wcd} (−22‰), $f_{assimilator}$ is still relatively low (0.24). In comparison, $f_{assimilator}$ in modern oceans is about 0.7 (see the Supplementary Materials). Thus, our integrated Fe speciation and nitrogen isotope data, coupled with numerical modeling results, suggest that the Xuhuai basin was probably characterized by ferruginous anoxia, a relatively small marine nitrate reservoir, and a relatively low contribution of nitrate assimilators to sedimentary nitrogen. Considering the global-scale shallow-water anoxia evidenced by uranium isotope data (56), the patterns we observed in the Xuhuai basin may be representative of the global ocean. If so, an inescapable implication is that nitrate-assimilating eukaryotes likely played a limited ecological role in early Tonian oceans.

Long-term $\delta^{15}N$ trend, nitrate availability, and ecological rise of eukaryotes

The compilation of sedimentary nitrogen isotope data (n = 1824) span the beginning of the Mesoproterozoic at 1.6 Ga, when acritarchs started to appear abundantly in the fossil record (1), to the end of the Neoproterozoic at ~0.539 Ga, when multicellular eukaryotes, including possible stem-group animals, became ecologically dominant (61).

We argue that the long-term trend in $\delta^{15}N$ values over this time interval can inform us about changes in the marine nitrogen cycle and nitrate availability. In particular, the lowest quartile of $\delta^{15}N$ data in each time bin is informative. We focus on the lowest quartile for two reasons: (i) It is likely more informative of the extent of nitrate-limited regions, and (ii) it helps us to better tackle the potential impact of diagenetic alteration. With regard to the first reason, there was likely greater spatial heterogeneity in nitrate concentrations in Proterozoic oceans relative to modern oceans, given that the average nitrate concentration was lower and the residence time was shorter. The residence time of fixed nitrogen in modern oceans is less than 2000 years (62). With stronger nitrogen loss through denitrification/anammox in Proterozoic oceans, the residence time may be shorter than the ocean mixing time, resulting in spatial heterogeneity in both nitrate availability and $\delta^{15}N$ values (e.g., figs. S6 and S7). Considering that oxic oases may
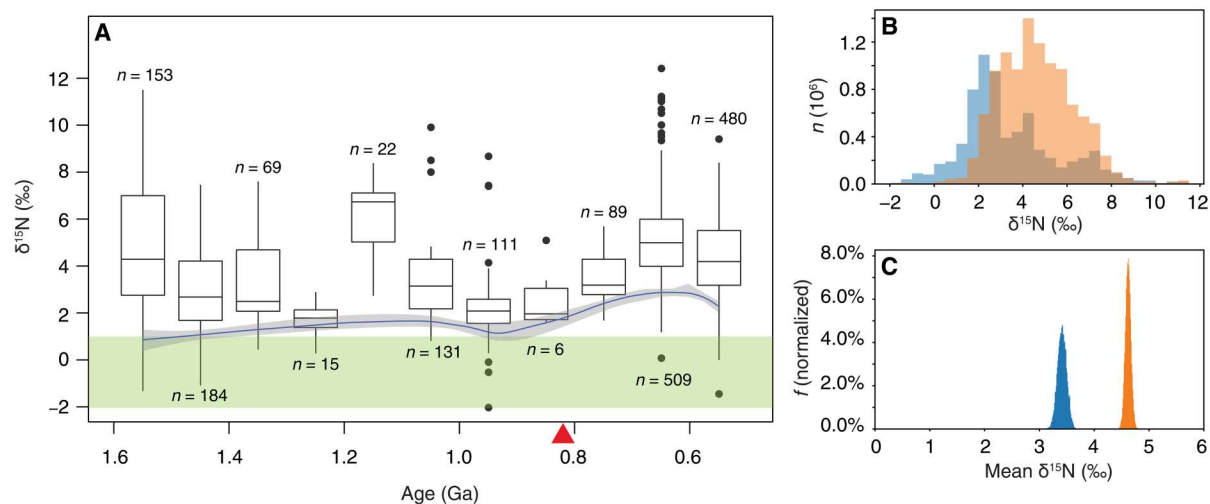
Fig. 6. Nitrogen isotope composition (δ^{15}N) of sedimentary rocks through time. (**A**) Compilation of published nitrogen isotope data from Mesoproterozoic to Neoproterozoic. Boxplots show distribution of δ^{15}N values in each 100-Ma time bin. Blue line is LOWESS regression fit of lowest 25% δ^{15}N data in every 100-Ma time bin; see fig. S6 for LOWESS regression fit of lowest 50% data and the entire dataset. Gray shade is 95% CI calculated from 10,000 bootstrapping experiments. Red triangle marks stepwise increase from a changepoint analysis of lowest 25% δ^{15}N data. Most significant change in both mean and variance occurs at ca. 820 Ma. The green shade marks δ^{15}N values characteristic of a nitrogen cycle dominated by nitrogen fixation (e.g., $f_{assimilator}$ < 0.16; see Fig. 5). (**B**) Frequency distributions of δ^{15}N values from bootstrapping experiments (n = 10,000) of pre–800 Ma (blue) and post–800 Ma (orange) samples. (**C**) Frequency distributions of mean δ^{15}N values from bootstrapping experiments (n = 10,000) of pre–800 Ma (blue) and post–800 Ma (orange) samples.

have been present in Mesoproterozoic oceans and nitrate supplies may have been locally abundant (*63*), such isotopic heterogeneity was likely accentuated. Because the focus of this study was on the ecological rise of eukaryotes on a global scale, we are more interested in time intervals and regions where nitrate availability could have limited eukaryote success, rather than local environments where eukaryotes may have managed to survive. As such, the lowest quartile of the δ^{15}N compilation is more informative of the extent of nitrate-limited regions. For the second reason, the lowest quartile helps us to better address the potential issue of diagenetic alteration. Some of the variations in the compiled δ^{15}N data may be related to diagenesis and metamorphism, which tend to elevate δ^{15}N values. Therefore, instead of tracking the temporal pattern of the entire dataset, we subjected the lowest quartile in each 100-Ma time bin to a locally weighted scatterplot smoothing (LOWESS) regression analysis to understand the long-term evolution of δ^{15}N (Fig. 6A). Nonetheless, as sensitivity tests and a validation of the trend captured by the lowest quartile data, we also conducted the same LOWESS regression on the lowest 50% data and the entire dataset (fig. S6). We would also like to note that δ^{15}N data from the terminal Ediacaran Period (551 to 539 Ma) were not included in the analysis because this interval is marked by a brief return to extensive oceanic anoxia (*64*) and thus a likely return to a more broadly nitrate-limited ocean. The terminal Ediacaran is characterized by rather low δ^{15}N values (*19*, *20*) and witnessed the extinction of both macro- and microscopic eukaryotes (*65*, *66*), perhaps representing a transient return to a prokaryote-dominant world ecologically akin to pre-Cryogenian oceans.

LOWESS analysis of the lowest quartile data revealed a stepwise increase in δ^{15}N values around 800 Ma, from less than 2 to ~3‰. The deviation in the 1.1- to 1.2-Ga time bin is probably related to sampling bias: data in this time bin come from only one section that was deposited in a well-oxygenated basin (*67*). Because of the

scarcity of data in the 800- to 900-Ma time bin, the bootstrapped LOWESS result indicates that the rise in δ^{15}N could have started as early as 900 Ma, but a changepoint detection analysis revealed that the most significant change in the mean and variance of the lowest 25% δ^{15}N data occurred at ca. 820 Ma (Fig. 6A). We note that more data from the 800- to 900-Ma time bin are needed to accurately define the rise of δ^{15}N. Sensitivity tests of LOWESS regression and changepoint detection analysis on the lowest 50% data and the entire dataset (fig. S6) also revealed a stepwise rise at around 800 Ma, although these analyses show more temporal variation. These analyses are further supported by a two-group analysis of the entire dataset: the mean δ^{15}N values of pre–800 Ma (3.4 ± 2.2‰) and post–800 Ma (4.6 ± 1.7‰) subdatasets are significantly different (P < 0.0001, Z test), and the difference remains statistically significant for the bootstrapped subdatasets (P < 0.0001, Z test) (Fig. 6, B and C). The post–800 Ma subgroup has slightly higher TN and TOC contents, but this difference is small, and therefore, the difference in δ^{15}N values is unlikely related to differences in either TOC or TN (fig. S8). Last, the variability of the bootstrapped δ^{15}N values is higher in the pre–800 Ma subdataset (Fig. 6, B and C), consistent with a smaller nitrate reservoir with greater spatial heterogeneity and temporal dynamics.

We can use the same box model described above to better assess the evolution of nitrate availability during the Mesoproterozoic and Neoproterozoic eras. For the lowest quartile of the compiled data, a rise in δ^{15}N from 2 to 3‰ at ~800 Ma indicates an increase in $f_{assimilator}$ from 0.11 [95% confidence interval (CI): 0.04 to 0.21, Monte Carlo simulation to account for uncertainty in ε_{fix} and ε_{wcd}] to 0.16 (95% CI: 0.08 to 0.31), suggesting a ~50% increase in $f_{assimilator}$ (Fig. 5). For the entire dataset, the mean δ^{15}N values of the pre– and post–800 Ma subgroups cannot be achieved with low ε_{fix} and high ε_{wcd} values. If the median values are used (ε_{fix} = −0.5‰ and ε_{wcd} = −26‰), an increase in average δ^{15}N from 3.4 to 4.6‰

implies a change in $f_{assimilator}$ from 0.18 to 0.27, again representing a ~50% increase. It should be emphasized that, because this box model does not capture spatial heterogeneity and temporal dynamics, the calculated 50% increase in nitrate burial flux represents a global average. If we assume a first-order relationship between the reservoir size and input/output fluxes, this change in nitrate burial flux represents a 50% increase in nitrate availability in the global ocean. Although the nitrate levels of post–800 Ma oceans may have remained low relative to that of modern oceans, this significant increase may have provided an important resource to support the proliferation of eukaryotic primary producers and other eukaryotes further downstream in the food chain.

We note that an increase in $\delta^{15}N$ values of sedimentary nitrogen can also be achieved, in principle, by a decrease in ε_{wcd} (i.e., greater fractionation during water-column denitrification/anammox). However, considering that nitrate concentration inserts a primary control on the scale of fractionation (55), lower ε_{wcd} values imply higher nitrate levels in the ocean. Thus, the main conclusion still holds that higher $\delta^{15}N_{sed}$ values imply greater nitrate availability.

The ultimate driver for a stepwise increase in marine nitrate availability at ~800 Ma is unclear. It is possible that this increase was caused by the rise of atmospheric oxygen levels at ~800 Ma, as indicated by the shale chromium isotope record [(25, 26), but see (68, 69)]. The breakup of the supercontinent Rodinia (70) and the rise of mountains (71) may have intensified continental weathering (38) and enhanced nutrient supply (e.g., phosphorus) into the ocean, which would incentivize nitrogen fixation to match the availability of other macronutrients, promoting the increase in primary productivity and the subsequent rise of oxygen levels in the atmosphere and shallow oceans. Oxic shallow waters would then weaken water-column denitrification and anammox, increasing nitrate availability and supporting eukaryotic primary producers. The ecological rise of eukaryotes, in turn, would lead to a more efficient biological pump, push the oxygen demand to greater depths, and deepen the chemocline (72), which would further increase the oceanic nitrate reservoir size. This positive feedback highlights the complex interactions among biological, atmospheric, oceanic, and tectonic processes that would have influenced the growth of the marine nitrate reservoir and the ecological rise of eukaryotes (Fig. 7).

To sum up, the Fe speciation and nitrogen isotope data reported here from the early Tonian Huaibei Group in the NCC fill an important gap in the oceanic redox proxy record of the Proterozoic. Together, the data indicate ferruginous conditions in shallow marine environments, where the contribution of nitrate-assimilating eukaryotes to sedimentary nitrogen was limited. A simple box model calculation indicates that, in the Huaibei basin, nitrate assimilators contributed ~10% to sedimentary nitrogen, compared with ~70% in modern oceans. With data from the Huaibei Group added to the compilation of Mesoproterozoic-Neoproterozoic $\delta^{15}N$ data, our analysis indicates a stepwise increase in sedimentary $\delta^{15}N$ values at ~800 Ma. This increase implies a ~50% increase in marine nitrate availability and eukaryotic contribution to sedimentary nitrogen. It is possible that tectonic, oceanic, atmospheric, and biological processes together shaped the history of marine redox conditions and nitrate supply, which, together with the increased availability of other nutrients such as phosphorus, supported the ecological rise of eukaryotes.

MATERIALS AND METHODS
Iron speciation
Fe_T was measured by heating ~0.3 g of powdered sample at 950°C for 6 to 8 hours and then dissolving the powder in concentrated hydrochloric acid at 140°C for 48 hours. Iron in carbonate (Fe_{carb}), iron oxides (Fe_{ox}), and magnetite (Fe_{mag}) were extracted from ~0.15 g of powdered sample following the sequential extraction method of Poulton and Canfield (73). The iron concentration of these extracted species was measured using the Ferrozine method (74) and analyzed on a Thermo Fisher Scientific GENESYS 10S UV-VIS spectrophotometer at Virginia Tech after they were left to react with the Ferrozine reagent for ~12 hours to ensure that the complexation reaction reached completion. Pyrite sulfur was extracted from ~5 g of powdered sample using the chromium reduction method (75), and its concentration was determined by gravimetry of the produced Ag_2S precipitate. Iron found in pyrite (Fe_{py}) was calculated using the stoichiometry of pyrite and the amount of pyrite sulfur extracted. The precision (1 SD, here and throughout) of the sequential iron extraction based on sample replicates and internal laboratory standards was ~8%. The precision of the gravimetric pyrite content analysis was ~6%, and Fe_T was ~5%.

Nitrogen and carbon isotopes
Samples were decarbonated using overnight digestion in 4 M hydrochloric acid and then centrifuged to separate the undissolved residue. The undissolved residue was then rinsed three times with 18.2 megohm·cm deionized water to remove any residual hydrochloric acid. The undissolved residue was dried at 50°C and then homogenized. An aliquot of 2 to 50 mg of decarbonated residue was weighed and packaged in a tin capsule for organic carbon isotope analysis; similarly, 50 to 200 mg of decarbonated residue was weighed for nitrogen isotope analysis. Carbon and nitrogen isotopic compositions were determined separately on an Isoprime 100 isotope ratio mass spectrometer coupled with an Elementar vario ISOTOPE cube elemental analyzer at Virginia Tech. For carbon isotope analysis, the temperature of the combustion column and the reduction column was set at 1050° and 650°C, respectively. For nitrogen isotope analysis, the combustion column was heated up to 1150°C, while the reduction column was kept at 650°C. Samples were normalized to the Vienna Pee Dee belemnite (VPDB) and Air scales using two-point linear normalization. CH-6 ($\delta^{13}C_{VPDB} = -10.45 \pm 0.03‰$), CH-7 ($\delta^{13}C_{VPDB} = -32.15 \pm 0.05‰$), Elemental Microanalysis Low Organic Content Soil ($\delta^{13}C_{VPDB} = -22.88 \pm 0.40‰$), and Elemental Microanalysis Wheat Flour ($\delta^{13}C_{VPDB} = -27.21 \pm 0.13‰$) were used as carbon isotope standards. USGS25 ($\delta^{15}N_{Air} = -30.41 \pm 0.16‰$), USGS26 ($\delta^{15}N_{Air} = 53.75 \pm 0.15‰$), and Elemental Microanalysis Urea ($\delta^{15}N_{Air} = -0.30 \pm 0.2‰$) were used as nitrogen isotope standards. The precision of organic carbon isotope analysis was 0.4‰ (1 SD, here and throughout), based on the repeated measurement of 11 Elemental Microanalysis Low Organic Content Soil standards and 5 Elemental Microanalysis Wheat Flour standards. $\delta^{13}C$ measurements of Elemental Microanalysis Low Organic Content Soil ($-23.0 \pm 0.5‰$) and Elemental Microanalysis Wheat Flour ($-27.5 \pm 0.1‰$) agree well with the expected values. The precision of nitrogen isotope analysis was 0.1‰, based on the repeated measurement of 16 Elemental Microanalysis Urea standards. $\delta^{15}N$ Measurements of Elemental Microanalysis Urea
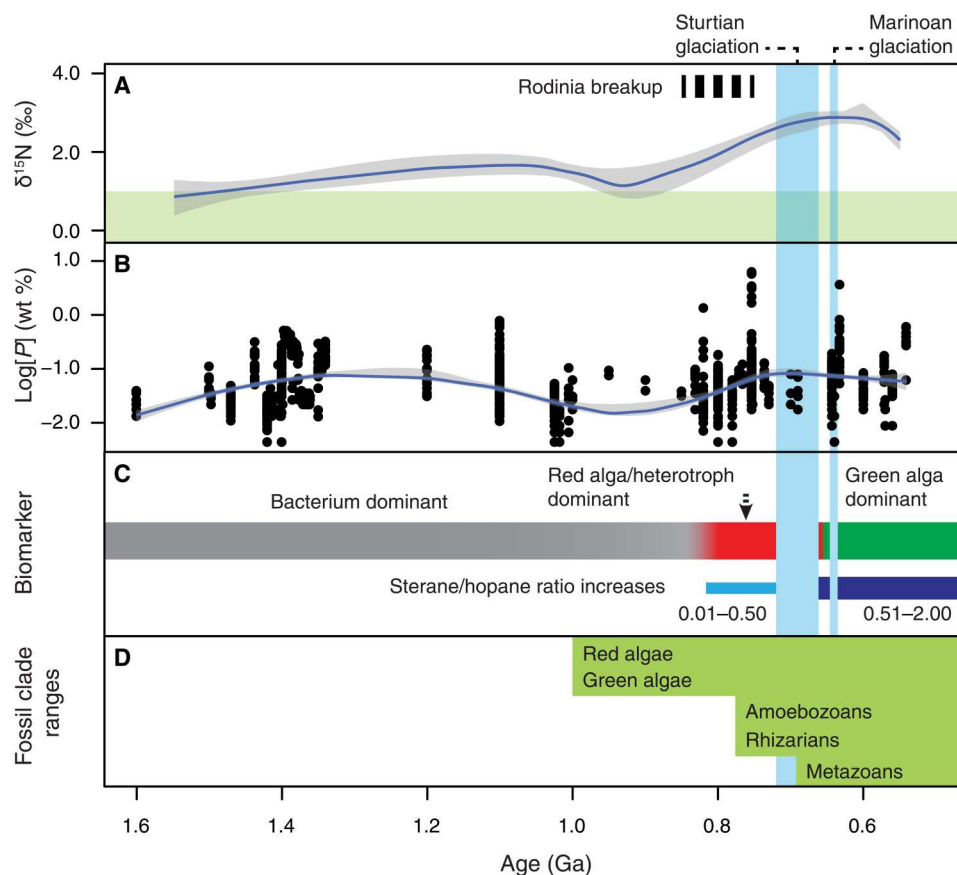
Fig. 7. Secular variations in δ^{15}N and phosphorus content, in comparison with biomarker and eukaryotic fossil record of the Mesoproterozoic and Neoproterozoic eras. (**A**) LOWESS regression curve of lowest 25% δ^{15}N data in every 100-Ma time bin. A stepwise rise in δ^{15}N at ca. 800 Ma coincides with breakup of supercontinent Rodinia and implies increasing marine nitrate availability. (**B**) Phosphorus concentrations of marine siliciclastic sediments through time (*13*, *79*). LOWESS regression is based on the entire dataset. An increase in late Tonian implies greater phosphorus availability in the surface ocean. (**C**) Biomarker data (see the Supplementary Materials) (*80*). Note oldest steranes at ca. 820 Ma, increasing sterane/hopane ratios, and inferred dominance of various primary producers. (**D**) Approximate stratigraphic ranges of major eukaryotic clades (*5*).

standards (-0.5 ± 0.1‰) agree well with the expected value. The reproducibility for δ^{15}N on duplicated samples ($n = 20$) was 0.4‰.

Nitrogen isotope data compilation

Published nitrogen isotope data have been screened and only samples below or near greenschist metamorphic grade that likely better reflect primary oceanic signals were included ($n = 1824$). As bulk nitrogen isotope values may be more accurate (*19*), δ^{15}N$_{bulk}$ data were prioritized when available ($n = 1759$); if δ^{15}N$_{bulk}$ data are not available, then kerogen nitrogen isotope data were used ($n = 65$).

Statistical analysis
Locally weighted scatterplot smoothing

LOWESS is a nonparametric, locally weighted regression method for smoothing scatterplots. It is ideal for analyzing time series plots with no theoretical functions. At each data point, a local polynomial with a fixed degree is fitted to the nearest f percentage of the dataset using weighted least squares. Data points within this f percentage of the dataset are weighted using the tri-cube weight function. More weight is given to points closer to the target point. We

used a polynomial degree of 2 to minimize bias. For the Huaibei Group data (Fig. 3D), we used an f value of 30%, and the CI was calculated from the SEs. For the compiled dataset (Fig. 6A), we used an f value of 50% to minimize local fluctuations and capture large-scale trends. To further minimize sampling bias, the data were bootstrapped 10,000 times, and LOWESS regression was performed each time. The 95% CI of the LOWESS regression was calculated on the basis of the 10,000 LOWESS regression curves. All LOWESS regression analyses were performed in the R Statistical Software using the spatialEco and loess packages (*76*).

Monte Carlo simulation

In this study, we assume a uniform distribution for ϵ_{fix} (from -2 to 1‰) and ϵ_{wcd} (from -30 to -22‰). Following the law of large numbers, values for ϵ_{fix} and ϵ_{wcd} were randomly drawn from these two uniform distributions to calculate the δ^{15}N$_{sed}$ value using the box model described in the text (fig. S2). This process was repeated 10,000 times to estimate the 95% CI of δ^{15}N$_{sed}$ (Fig. 5E).

Changepoint detection

For the time series data, changepoint detection aims to estimate the point at which the statistical properties of this dataset change based

on the likelihood test statistics (*77*). In this study, we focused on change in both the mean and variance of the $\delta^{15}N$ dataset. The analysis was performed in R Statistical Software using the changepoint package (*77*). We assumed a normal distribution of the data. The default Modified Bayes Information Criterion penalty was used to find the cutoff point, and the AMOC (at most one change) method was used to detect the most significant change point.

Supplementary Materials

This PDF file includes:
Supplementary Text
Figs. S1 to S8
Tables S1 and S2
Legends for data S1 to S3
References

Other Supplementary Material for this manuscript includes the following:
Data files S1 to S3

REFERENCES AND NOTES

1. P. A. Cohen, R. B. Kodner, The earliest history of eukaryotic life: Uncovering an evolutionary story through the integration of biological and geological data. *Trends Ecol. Evol.* **37**, 246–256 (2022).

2. S. M. Porter, Insights into eukaryogenesis from the fossil record. *Interface Focus* **10**, 20190105 (2020).

3. D. B. Mills, R. A. Boyle, S. J. Daines, E. A. Sperling, D. Pisani, P. C. J. Donoghue, T. M. Lenton, Eukaryogenesis and oxygen in Earth history. *Nat. Ecol. Evol.* **6**, 520–532 (2022).

4. S. Xiao, Q. Tang, After the boring billion and before the freezing millions: Evolutionary patterns and innovations in the Tonian Period. *Emerg. Top. Life Sci.* **2**, 161–171 (2018).

5. P. A. Cohen, L. A. Riedman, It's a protist-eat-protist world: Recalcitrance, predation, and evolution in the Tonian–Cryogenian ocean. *Emerg. Top. Life Sci.* **2**, 173–180 (2018).

6. J. W. Huntley, S. Xiao, M. Kowalewski, 1.3 Billion years of acritarch history: An empirical morphospace approach. *Precambrian Res.* **144**, 52–68 (2006).

7. J. J. Brocks, A. J. M. Jarrett, E. Sirantoine, C. Hallmann, Y. Hoshino, T. Liyanage, The rise of algae in Cryogenian oceans and the emergence of animals. *Nature* **548**, 578–581 (2017).

8. L. K. Eckford-Soper, K. H. Andersen, T. F. Hansen, D. E. Canfield, A case for an active eukaryotic marine biosphere during the Proterozoic era. *Proc. Natl. Acad. Sci. U.S.A.* **119**, e2122042119 (2022).

9. J. W. Huntley, M. Kowalewski, Strong coupling of predation intensity and diversity in the Phanerozoic fossil record. *Proc. Natl. Acad. Sci. U.S.A.* **104**, 15006–15010 (2007).

10. J. R. Meyer, R. Kassen, The effects of competition and predation on diversification in a model adaptive radiation. *Nature* **446**, 432–435 (2007).

11. S. Porter, The rise of predators. *Geology* **39**, 607–608 (2011).

12. T. Tyrrell, The relative influences of nitrogen and phosphorus on oceanic primary production. *Nature* **400**, 525–531 (1999).

13. C. T. Reinhard, N. J. Planavsky, B. C. Gill, K. Ozaki, L. J. Robbins, T. W. Lyons, W. W. Fischer, C. Wang, D. B. Cole, K. O. Konhauser, Evolution of the global phosphorus cycle. *Nature* **541**, 386–389 (2017).

14. M. A. Kipp, E. E. Stüeken, Biomass recycling and Earth's early phosphorus cycle. *Sci. Adv.* **3**, eaao4795 (2017).

15. C. T. Reinhard, N. J. Planavsky, B. A. Ward, G. D. Love, G. le Hir, A. Ridgwell, The impact of marine nutrient abundance on early eukaryotic ecosystems. *Geobiology* **18**, 139–151 (2020).

16. N. J. Planavsky, O. J. Rouxel, A. Bekker, S. V. Lalonde, K. O. Konhauser, C. T. Reinhard, T. W. Lyons, The evolution of the marine phosphate reservoir. *Nature* **467**, 1088–1090 (2010).

17. P. G. Falkowski, Evolution of the nitrogen cycle and its influence on the biological sequestration of CO_2 in the ocean. *Nature* **387**, 272–275 (1997).

18. J. Füssel, P. Lam, G. Lavik, M. M. Jensen, M. Holtappels, M. Günter, M. M. M. Kuypers, Nitrite oxidation in the Namibian oxygen minimum zone. *ISME J.* **6**, 1200–1209 (2012).

19. E. E. Stüeken, M. A. Kipp, M. C. Koehler, R. Buick, The evolution of Earth's biogeochemical nitrogen cycle. *Earth Sci. Rev.* **160**, 220–239 (2016).

20. M. Ader, C. Thomazo, P. Sansjofre, V. Busigny, D. Papineau, R. Laffont, P. Cartigny, G. P. Halverson, Interpretation of the nitrogen isotopic composition of Precambrian sedimentary rocks: Assumptions and perspectives. *Chem. Geol.* **429**, 93–110 (2016).

21. A. D. Anbar, A. H. Knoll, Proterozoic ocean chemistry and evolution: A bioinorganic bridge? *Science* **297**, 1137–1142 (2002).

22. J. A. Sohm, E. A. Webb, D. G. Capone, Emerging patterns of marine nitrogen fixation. *Nat. Rev. Microbiol.* **9**, 499–508 (2011).

23. S. E. Fawcett, M. W. Lomas, J. R. Casey, B. B. Ward, D. M. Sigman, Assimilation of upwelled nitrate by small eukaryotes in the Sargasso Sea. *Nat. Geosci.* **4**, 717–722 (2011).

24. Q. Dortch, J. Clayton, S. Thoresen, S. Ahmed, Species differences in accumulation of nitrogen pools in phytoplankton. *Mar. Biol.* **81**, 237–250 (1984).

25. N. J. Planavsky, C. T. Reinhard, X. Wang, D. Thomson, P. McGoldrick, R. H. Rainbird, T. Johnson, W. W. Fischer, T. W. Lyons, Low mid-Proterozoic atmospheric oxygen levels and the delayed rise of animals. *Science* **346**, 635–638 (2014).

26. D. B. Cole, C. T. Reinhard, X. Wang, B. Gueguen, G. P. Halverson, T. Gibson, M. S. W. Hodgskiss, N. R. McKenzie, T. W. Lyons, N. J. Planavsky, A shale-hosted Cr isotope record of low atmospheric oxygen during the Proterozoic. *Geology* **44**, 555–558 (2016).

27. R. Guilbaud, S. W. Poulton, N. J. Butterfield, M. Zhu, G. A. Shields-Zhou, A global transition to ferruginous conditions in the early Neoproterozoic oceans. *Nat. Geosci.* **8**, 466–470 (2015).

28. K. Fennel, M. Follows, P. G. Falkowski, The co-evolution of the nitrogen, carbon and oxygen cycles in the Proterozoic ocean. *Am. J. Sci.* **305**, 526–545 (2005).

29. J. E. Tesdal, E. D. Galbraith, M. Kienast, Nitrogen isotopes in bulk marine sediment: Linking seafloor observations with subseafloor records. *Biogeosciences* **10**, 101–118 (2013).

30. E. E. Stüeken, A test of the nitrogen-limitation hypothesis for retarded eukaryote radiation: Nitrogen isotopes across a Mesoproterozoic basinal profile. *Geochim. Cosmochim. Acta* **120**, 121–139 (2013).

31. S. Xiao, B. Shen, Q. Tang, A. J. Kaufman, X. Yuan, J. Li, M. Qian, Biostratigraphic and chemostratigraphic constraints on the age of early Neoproterozoic carbonate successions in North China. *Precambrian Res.* **246**, 208–225 (2014).

32. B. Wan, Q. Tang, K. Pang, X. Wang, Z. Bao, F. Meng, C. Zhou, X. Yuan, H. Hua, S. Xiao, Repositioning the Great Unconformity at the southeastern margin of the North China Craton. *Precambrian Res.* **324**, 1–17 (2019).

33. Q. Tang, K. Pang, X. Yuan, B. Wan, S. Xiao, Organic-walled microfossils from the Tonian Gouhou Formation, Huaibei region, North China Craton, and their biostratigraphic implications. *Precambrian Res.* **266**, 296–318 (2015).

34. Z. Li, D. Liu, X. Wu, G. Wang, T. Wang, Hydrocarbon-generating potentials of the Neoproterozoic in Xuhuai area, the east part of southern North China. *Chin. J. Geol.* **47**, 154–168 (2012).

35. K. Pang, Q. Tang, C. Wu, G. Li, L. Chen, B. Wan, X. Yuan, R. J. Bodnar, S. Xiao, Raman spectroscopy and structural heterogeneity of carbonaceous material in Proterozoic organic-walled microfossils in the North China Craton. *Precambrian Res.* **346**, 105818 (2020).

36. S. Zhang, R. Cao, Z. Lan, Z. Li, Z. Zhao, B. Wan, C. Guan, X. Yuan, SIMS Pb-Pb dating of phosphates in the Proterozoic strata of SE North China Craton: Constraints on eukaryote evolution. *Precambrian Res.* **371**, 106562 (2022).

37. X. Su, P. Peng, S. Foley, W. Teixeira, M.-G. Zhai, Initiation of continental breakup documented in evolution of the magma plumbing system of the ca. 925 Ma Dashigou large igneous province, North China. *Lithos* **384**, 105984 (2021).

38. Y. Zhou, P. A. E. Pogge von Strandmann, M. Zhu, H. Ling, C. Manning, D. Li, T. He, G. A. Shields, Reconstructing Tonian seawater 87Sr/86Sr using calcite microspar. *Geology* **48**, 462–467 (2020).

39. D.-B. Yang, W. L. Xu, Y. G. Xu, Q. H. Wang, F. P. Pei, F. Wang, U–Pb ages and Hf isotope data from detrital zircons in the Neoproterozoic sandstones of northern Jiangsu and southern Liaoning Provinces, China: Implications for the Late Precambrian evolution of the southeastern North China Craton. *Precambrian Res.* **216-219**, 162–176 (2012).

40. F. Sun, P. Peng, X. Zhou, A. J. C. Magalhães, F. Guadagnin, X. Zhou, Z. Zhang, X. Su, Provenance analysis of the late Mesoproterozoic to Neoproterozoic Xuhai Basin in the southeast North China Craton: Implications for paleogeographic reconstruction. *Precambrian Res.* **337**, 105554 (2020).

41. L. Wang, "Stratigraphic division, correlation and sedimentary environment analysis of the Neoproterozoic in Xuhuai region," thesis, Shandong University of Science and Technology, Shandong, China (2009).

42. R. Raiswell, D. S. Hardisty, T. W. Lyons, D. E. Canfield, J. D. Owens, N. J. Planavsky, S. W. Poulton, C. T. Reinhard, The iron paleoredox proxies: A guide to the pitfalls, problems and proper practice. *Am. J. Sci.* **318**, 491–526 (2018).

43. T. W. Lyons, S. Severmann, A critical look at iron paleoredox proxies: New insights from modern euxinic marine basins. *Geochim. Cosmochim. Acta* **70**, 5698–5722 (2006).

44. A. Benkovitz, A. Matthews, N. Teutsch, S. W. Poulton, M. Bar-Matthews, A. Almogi-Labin, Tracing water column euxinia in Eastern Mediterranean Sapropels S5 and S7. *Chem. Geol.* **545**, 119627 (2020).

45. S. W. Poulton, The iron speciation paleoredox proxy, in *Elements in Geochemical Tracers in Earth System Science*, T. Lyons, A. Turchyn, C. Reinhard, Eds. (Cambridge Univ. Press, 2021), pp. 1–28.

46. M. O. Clarkson, S. W. Poulton, R. Guilbaud, R. A. Wood, Assessing the utility of Fe/Al and Fe-speciation to record water column redox conditions in carbonate-rich sediments. *Chem. Geol.* **382**, 111–122 (2014).

47. A. K. Garcia, H. McShea, B. Kolaczkowski, B. Kaçar, Reconstructing the evolutionary history of nitrogenases: Evidence for ancestral molybdenum-cofactor utilization. *Geobiology* **18**, 394–411 (2020).

48. B. Marty, L. Zimmermann, M. Pujol, R. Burgess, P. Philippot, Nitrogen isotopic composition and density of the Archean atmosphere. *Science* **342**, 101–104 (2013).

49. A. H. Devol, Denitrification, anammox, and N_2 production in marine sediments. *Annu. Rev. Mar. Sci.* **7**, 403–423 (2015).

50. T. Algeo, P. Meyers, R. S. Robinson, H. Rowe, G. Jiang, Icehouse–greenhouse variations in marine denitrification. *Biogeosciences* **11**, 1273–1295 (2014).

51. M. A. Kipp, E. E. Stüeken, M. Yun, A. Bekker, R. Buick, Pervasive aerobic nitrogen cycling in the surface ocean across the Paleoproterozoic Era. *Earth Planet. Sci. Lett.* **500**, 117–126 (2018).

52. C. C. Michiels, F. Darchambeau, F. A. E. Roland, C. Morana, M. Llirós, T. García-Armisen, B. Thamdrup, A. V. Borges, D. E. Canfield, P. Servais, J. P. Descy, S. A. Crowe, Iron-dependent nitrogen cycling in a ferruginous lake and the nutrient status of Proterozoic oceans. *Nat. Geosci.* **10**, 217–221 (2017).

53. D. E. Canfield, B. B. Jørgensen, H. Fossing, R. Glud, J. Gundersen, N. B. Ramsing, B. Thamdrup, J. W. Hansen, L. P. Nielsen, P. O. J. Hall, Pathways of organic carbon oxidation in three continental margin sediments. *Mar. Geol.* **113**, 27–40 (1993).

54. B. Brunner, S. Contreras, M. F. Lehmann, O. Matantseva, M. Rollog, T. Kalvelage, G. Klockgether, G. Lavik, M. S. M. Jetten, B. Kartal, M. M. M. Kuypers, Nitrogen isotope effects induced by anammox bacteria. *Proc. Natl. Acad. Sci. U.S.A.* **110**, 18994–18999 (2013).

55. K. Kritee, D. M. Sigman, J. Granger, B. B. Ward, A. Jayakumar, C. Deutsch, Reduced isotope fractionation by denitrification under conditions relevant to the ocean. *Geochim. Cosmochim. Acta* **92**, 243–259 (2012).

56. F. Zhang, R. G. Stockey, S. Xiao, S. Z. Shen, T. W. Dahl, G. Y. Wei, M. Cao, Z. Li, J. Kang, Y. Cui, A. D. Anbar, N. J. Planavsky, Uranium isotope evidence for extensive shallow water anoxia in the early Tonian oceans. *Earth Planet. Sci. Lett.* **583**, 117437 (2022).

57. A. M. Hutchings, A. V. Turchyn, A quantification of the effect of diagenesis on the paleo-redox record in mid-Proterozoic sedimentary rocks. *Geology* **49**, 1143–1147 (2021).

58. A. van Smeerdijk Hood, M. W. Wallace, Synsedimentary diagenesis in a Cryogenian reef complex: Ubiquitous marine dolomite precipitation. *Sediment. Geol.* **255–256**, 56–71 (2012).

59. J. Kang, C. Li, L. Dong, S. Xiao, Early diagenetic dolomite as a potential archive of paleo-redox fluctuations in an early Tonian marine basin? *Acta Geol. Sin.* **96**, 607–620 (2022).

60. P. Müller, CN ratios in Pacific deep-sea sediments: Effect of inorganic ammonium and organic nitrogen compounds sorbed by clays. *Geochim. Cosmochim. Acta* **41**, 765–776 (1977).

61. S. Xiao, M. Laflamme, On the eve of animal radiation: Phylogeny, ecology and evolution of the Ediacara biota. *Trends Ecol. Evol.* **24**, 31–40 (2009).

62. J. A. Brandes, A. H. Devol, A global marine-fixed nitrogen isotopic budget: Implications for Holocene nitrogen cycling. *Global Biogeochem. Cycles* **16**, 67-1–67-14 (2002).

63. Z. Wang, X. Wang, X. Shi, D. Tang, E. E. Stüeken, H. Song, Coupled nitrate and phosphate availability facilitated the expansion of eukaryotic life at circa 1.56 Ga. *J. Geophys. Res. Biogeosci.* **125**, e2019JG005487 (2020).

64. F. Zhang, S. Xiao, B. Kendall, S. J. Romaniello, H. Cui, M. Meyer, G. J. Gilleaudeau, A. J. Kaufman, A. D. Anbar, Extensive marine anoxia during the terminal Ediacaran Period. *Sci. Adv.* **4**, eaan8983 (2018).

65. A. V. Kolesnikov, V. V. Marusin, K. E. Nagovitsin, A. V. Maslov, D. V. Grazhdankin, Ediacaran biota in the aftermath of the Kotlinian Crisis: Asha Group of the South Urals. *Precambrian Res.* **263**, 59–78 (2015).

66. S. D. Evans, C. Tu, A. Rizzo, R. L. Surprenant, P. C. Boan, H. McCandless, N. Marshall, S. Xiao, M. L. Droser, Environmental drivers of the first major animal extinction across the Ediacaran White Sea-Nama transition. *Proc. Natl. Acad. Sci. U.S.A.* **119**, e2207475119 (2022).

67. E. E. Stüeken, S. Viehmann, S. V. Hohl, Contrasting nutrient availability between marine and brackish waters in the late Mesoproterozoic: Evidence from the Paranoá Group, Brazil. *Geobiology* **20**, 159–174 (2022).

68. G. J. Gilleaudeau, R. Frei, A. J. Kaufman, L. C. Kah, K. Azmy, J. K. Bartley, P. Chernyavskiy, A. H. Knoll, Oxygenation of the mid-Proterozoic atmosphere: Clues from chromium isotopes in carbonates. *Geochem. Perspect. Lett.* **2**, 178–187 (2016).

69. D. E. Canfield, S. Zhang, A. B. Frank, X. Wang, H. Wang, J. Su, Y. Ye, R. Frei, Highly fractionated chromium isotopes in Mesoproterozoic-aged shales and atmospheric oxygen. *Nat. Commun.* **9**, 2871 (2018).

70. Z. X. Li, S. V. Bogdanova, A. S. Collins, A. Davidson, B. de Waele, R. E. Ernst, I. C. W. Fitzsimons, R. A. Fuck, D. P. Gladkochub, J. Jacobs, K. E. Karlstrom, S. Lu, L. M. Natapov, V. Pease, S. A. Pisarevsky, K. Thrane, V. Vernikovsky, Assembly, configuration, and break-up history of Rodinia: A synthesis. *Precambrian Res.* **160**, 179–210 (2008).

71. M. Tang, X. Chu, J. Hao, B. Shen, Orogenic quiescence in Earth's middle age. *Science* **371**, 728–731 (2021).

72. T. M. Lenton, R. A. Boyle, S. W. Poulton, G. A. Shields-Zhou, N. J. Butterfield, Co-evolution of eukaryotes and ocean oxygenation in the Neoproterozoic era. *Nat. Geosci.* **7**, 257–265 (2014).

73. S. W. Poulton, D. E. Canfield, Development of a sequential extraction procedure for iron: Implications for iron partitioning in continentally derived particulates. *Chem. Geol.* **214**, 209–221 (2005).

74. L. L. Stookey, Ferrozine—A new spectrophotometric reagent for iron. *Anal. Chem.* **42**, 779–781 (1970).

75. D. E. Canfield, R. Raiswell, J. T. Westrich, C. M. Reaves, R. A. Berner, The use of chromium reduction in the analysis of reduced inorganic sulfur in sediments and shales. *Chem. Geol.* **54**, 149–155 (1986).

76. J. S. Evans, spatialEco (2021).

77. R. Killick, I. Eckley, changepoint: An R package for changepoint analysis. *J. Stat. Softw.* **58**, 1–19 (2014).

78. W. Gregg, C. Rousseaux, NASA Ocean Biogeochemical Model assimilating satellite chlorophyll data global monthly VR2017 (Goddard Earth Sciences Data and Information Services Center, 2017).

79. N. J. Planavsky, D. Asael, A. D. Rooney, L. J. Robbins, B. C. Gill, C. M. Dehler, D. B. Cole, S. M. Porter, G. D. Love, K. O. Konhauser, C. T. Reinhard, A sedimentary record of the evolution of the global marine phosphorus cycle. *Geobiology* **21**, 168–174 (2023).

80. J. A. Zumberge, D. Rocher, G. D. Love, Free and kerogen-bound biomarkers from late Tonian sedimentary rocks record abundant eukaryotes in mid-Neoproterozoic marine communities. *Geobiology* **18**, 326–347 (2020).

81. S. Zhang, J. Su, S. Ma, H. Wang, X. Wang, K. He, H. Wang, D. E. Canfield, Eukaryotic red and green algae populated the tropical ocean 1400 million years ago. *Precambrian Res.* **357**, 106166 (2021).

82. T. T. Isson, G. D. Love, C. L. Dupont, C. T. Reinhard, A. J. Zumberge, D. Asael, B. Gueguen, J. McCrow, B. C. Gill, J. Owens, R. H. Rainbird, A. D. Rooney, M. Y. Zhao, E. E. Stueeken, K. O. Konhauser, S. G. John, T. W. Lyons, N. J. Planavsky, Tracking the rise of eukaryotes to ecological dominance with zinc isotopes. *Geobiology* **16**, 341–352 (2018).

83. W. W. Gregg, N. W. Casey, Modeling coccolithophores in the global oceans. *Deep-Sea Res. II Top. Stud. Oceanogr.* **54**, 447–477 (2007).

84. W. W. Gregg, P. Ginoux, P. S. Schopf, N. W. Casey, Phytoplankton and iron: Validation of a global three-dimensional ocean biogeochemical model. *Deep-Sea Res. II Top. Stud. Oceanogr.* **50**, 3143–3169 (2003).

85. H. Zhao, S. Zhang, J. Ding, L. Chang, Q. Ren, H. Li, T. Yang, H. Wu, New geochronologic and paleomagnetic results from early Neoproterozoic mafic sills and late Mesoproterozoic to early Neoproterozoic successions in the eastern North China Craton, and implications for the reconstruction of Rodinia. *GSA Bull.* **132**, 739–766 (2020).

86. R.-Z. Zhu, R. Ni, G. G. Wang, J. Y. Ding, M. S. Fan, Y. G. Ma, Geochronology, geochemistry and petrogenesis of the Laozhaishan dolerite sills in the southeastern margin of the North China Craton and their geological implication. *Gondw. Res.* **67**, 131–146 (2019).

87. T. He, Y. Zhou, P. Vermeesch, M. Rittner, L. Miao, M. Zhu, A. Carter, P. A. E. Pogge von Strandmann, G. A. Shields, Measuring the 'Great Unconformity' on the North China Craton using new detrital zircon age data. *Geol. Soc. Lond. Spec. Publ.* **448**, 145–159 (2016).

88. X. Fu, S. Zhang, H. Li, J. Ding, H. Li, T. Yang, H. Wu, H. Yuan, J. Lv, New paleomagnetic results from the Huaibei Group and Neoproterozoic mafic sills in the North China Craton and their paleogeographic implications. *Precambrian Res.* **269**, 90–106 (2015).

89. T. W. Lyons, J. P. Werne, D. J. Hollander, R. Murray, Contrasting sulfur geochemistry and Fe/Al and Mo/Al ratios across the last oxic-to-anoxic transition in the Cariaco Basin, Venezuela. *Chem. Geol.* **195**, 131–157 (2003).

90. C. März, S. W. Poulton, B. Beckmann, K. Küster, T. Wagner, S. Kasten, Redox sensitivity of P cycling during marine black shale formation: Dynamics of sulfidic and anoxic, non-sulfidic bottom waters. *Geochim. Cosmochim. Acta* **72**, 3703–3717 (2008).

91. C. Jin, C. Li, T. J. Algeo, N. J. Planavsky, H. Cui, X. Yang, Y. Zhao, X. Zhang, S. Xie, A highly redox-heterogeneous ocean in South China during the early Cambrian (~529–514 Ma): Implications for biota-environment co-evolution. *Earth Planet. Sci. Lett.* **441**, 38–51 (2016).

92. L. Xiang, S. D. Schoepfer, S.-z. Shen, C.-q. Cao, H. Zhang, Evolution of oceanic molybdenum and uranium reservoir size around the Ediacaran–Cambrian transition: Evidence from western Zhejiang, South China. *Earth Planet. Sci. Lett.* **464**, 84–94 (2017).

93. C. Li, N. J. Planavsky, G. D. Love, C. T. Reinhard, D. Hardisty, L. Feng, S. M. Bates, J. Huang, Q. Zhang, X. Chu, T. W. Lyons, Marine redox conditions in the middle Proterozoic ocean and isotopic constraints on authigenic carbonate formation: Insights from the Chuanlinggou Formation, Yanshan Basin, North China. *Geochim. Cosmochim. Acta* **150**, 90–105 (2015).